Wind Tunnel Measurements of Simulated Glaciated Cloud Conditions to Evaluate Newly Developed 2D Imaging Probes

Biagio M. Esposito CIRA, Italian Aerospace Research Centre

William D. Bachalo Artium Technologies Inc.

Delphine Leroy CNRS

Alfons Schwarzenboeck LaMP, Laboratoire de Météorologie Physiq

Tina Jurkat and Christiane Voigt DLR, German Aerospace Center

Stephan Bansmer Technische Universität Braunschweig

Abstract

Instrumentation that has been used for characterization of mixed-phase and glaciated conditions in the past, like the OAP probes, are subject to errors caused by variations in diffraction on the images away from the object plane and by the discrete nature of their particle detection and sizing. Correction methods are necessary to consider their measurements adequate for high ice water content (IWC) environments judged to represent a significant safety hazard to propellers and turbofan engine operability and performance. For this reason, within the frame of EU FP7 HAIC project, instrumentation characterization and validation is considered a major element need for successful execution of flight tests campaigns. Clearly, instrumentation must be sufficiently reliable to assess the reproducibility of artificial clouds with high ice water content generated in icing tunnels. Instruments are required to measure these conditions with a sufficient level of accuracy for the purposes of the testing. Currently, there is an anticipated basic uncertainty of a factor of 2-5 when measuring clouds in-situ. This may be worse for thunderstorm core regions, because of the poorly measured ice particle sizes below 100 µm when using legacy instruments. Measurements below 100 µm are especially difficult for ice particles. In order to mitigate this measurement limitation, an innovative approach for imaging droplets and ice crystals was considered in this work. This method is based on Artium Technologies Inc. High Speed Imaging (HSI) instrument. The method utilizes a unique multi-beam illumination approach to control the depth of field, minimize out-of-focus image noise effects, and limit obscuration of particles in the sample volume produced by out-of-focus particles in the optical path. Rather than utilizing a linear array to acquire the images, a modern CMOS two-dimensional array imaging system is used. The lasers used for producing bright field shadow images are pulsed synchronously and have pulse duration of as little as 12.5 ns to "freeze" the particle motion. The response of the HSI will be reviewed on the basis of comparison with SPEC 2D-S by means of wind tunnel measurements for glaciated cloud conditions.

Introduction

Measurements below 100 µm are difficult for ice particles. Older PMS OAPs have poor accuracy due to low resolution digitization, out-of-focus particles, response time, and sample volume uncertainty [1, 2, 3, 4, 5, 6]. Accurate measurement of ice particles smaller than 100 µm may be a critical issue for accurate estimations of MMD especially if most IWC mass are concentrated below 100 µm. Measurements of small crystals near the tops of very high, cold tropical cirrus clouds are reported to show very high concentrations (>10 cm^{-3}) of small crystals. However, results of these data [7] suggest that much of the existing database of cirrus measurements of small crystals may be suspect because of the shattering problem, at least under some conditions.

This situation motivates the need to evaluate newly developed 2D imaging probes that are designed to reduce the effect of shattering artifacts, and limit uncertainty due to out-of-focus images. Possible sources of error caused by the depth of field effect are the ambiguity of defining the particle boundaries for out-of-focus images, and the dependency of the depth of field

on particle size [3]. Size ambiguity increases for droplets and particles passing farther from the focal plane. It is known that the depth of field for acceptable focus decreases significantly with particle size. Small particles will appear to be out of focus at smaller distances from the focal plane than larger particles. Change in depth-of-field has been shown to vary almost linearly with drop size. This effect is also known to bias the counting of the particles towards the larger size images. In general, the size distribution will be biased and must be corrected for this change in depth-of-field with particle size.

A representative set of instruments used during HAIC flight tests (Darwin 2014, Cayenne 2016, Darwin/Réunion 2016) and wind tunnel measurements (Braunschweig, Esterline, DGA, GKN) of high Ice Water Content (IWC) cloud conditions have been inter-compared in the icing wind tunnel at the University of Braunschweig.

Wind tunnel tests were performed with four 2D imaging probes sampling cloud particles with a main objective of characterizing their response to glaciated conditions generated at different levels of Ice Water Content (IWC) and respective small Median Mass Diameters (MMD).

Wind tunnel test facilities are important for characterization of aircraft instrumentation and scientific airborne instruments detecting IWC at variable atmospheric conditions. The Technical University of Braunschweig provided within the HAIC project a new facility to enable testing a series of instruments in glaciated cloud conditions [8]. One important aspect that is unique for this new wind tunnel is the vapor grown ice generation that allows studying potentially more realistic (similar to ice crystals encountered in the free atmosphere) ice crystal populations within wind tunnel applications. The primary scope of this work is to provide the results of inter-comparison between the "standard" imaging probe (2D-S) and newly developed HSI probe.

As part of this study, the IWC and MMD nominal values were formerly studied with the IKP probe from Cranfield University and with the C-HSI from CIRA. The so far unknown MMD of crystals produced for the tunnel were examined, and accuracies were estimated and reported [11]. In general, MMD retrieval from 2D image's is not straightforward due to the lack of information of the third dimension of the ice crystals. Particularly within HAIC, several methodologies have been developed (for example, optimization of an inverse problem formulation or the dynamic retrieval of the mass size relationship from image analysis, number PSD, and simultaneous IWC measurements) [9]. For the wind tunnel measurements with cloud particle imagers, it was necessary to limit the mass-size relation to some constant relationships taken from literature [10] due to the lack of simultaneous IWC measurements from C-IKP that would be needed to constrain a more sophisticated calculation of the **m (D)** relationship. MMD estimates are particularly sensitive to the PSD number size distribution, to chosen diameter definition (D_{max}, D_{eq}, D_y, D_x, D_{mean}, D_{Feret}…), and the estimated/selected mass-size relationship [9, 20]. MMD may also depend on the to theused instrument, the image processing software used for retrieval of the number PSD, and to possible variations (question of reproducibility) of crystal properties produced for the Braunschweig wind tunnel (possible impact of ageing of stored ice, sieve performance, cloud inhomogeneity, etc. …) [11].

The 2D-S spectrometers (from SPEC Inc.) have been provided by both the CNRS-LaMP and DLR. The aim was to analyze sequentially the same nominal wind tunnel conditions, with different probes of the same type and also different data processing approaches. This allows verifying potential differences between two 2D-S probes due to potential wind tunnel conditions variability (repeatability check) as well as the effect produced by two different software versions to process the 2D-S imaging data. The last aspect is outside the scope of this article. The novel HSI technique from Artium Technologies Inc. was provided by CIRA as the in-situ probe in canister version (C-HSI). CNRS-LaMP 2D-S has been used for all the HAIC in-flight campaigns [12] while CIRA C-HSI was only used for Cayenne's in-flight campaign. Besides the in-situ probes, a modular version of HSI (M-HSI) was also provided to allow non-intrusive measurements upstream of each probe installed in the test section to assess the repeatability of the cloud's conditions. This version of the HSI has a large working distance (300 mm) sufficient to allow measurements on tunnel centerline from outside of the tunnel. In addition to these systems, a modular Phase Doppler Interferometer (PDI) was used with the purpose of monitoring the ice crystals' velocity close to the 2D-S sampling volume. The instruments compared the measurements of microphysical parameters with focus on particle number and size, derived IWC, and MMD. These parameters were compared and used to derive measured IWC from former IKP studies executed also for the same wind tunnel conditions considered in the defined test matrix. The main focus of this study was focused on glaciated icing conditions and temperatures below 0°C. The velocity of the particles, crucial to the derivation of the microphysical parameters, was additionally monitored with the PDI. Different optical set-ups, as well as computational IWC retrieval methods, were assessed.

Experimental Description

The experiment has been conducted at TU-BS closed loop icing wind tunnel, a brand-new small facility with an innovative ice crystal generation method based on cloud chamber technology which is able to replicate quite similar natural ice crystals during the tests. The test section size is approximately H 50 cm x W 50 cm where it is possible to achieve maximum airflow of 40 m s^{-1} and minimum static air temperature of -20 °C. For these tests, ice crystals were injected into the tunnel through a delivery pipe located near the center of the settling chamber. TU-BS roughly estimated potential IWC gradients over the wind tunnel cross section (Figure 1) thereby using a series of ice capture cylinders across the largest part of the test section. Spatially inhomogeneous ice distributions resulted from the single ice crystals delivery pipe and respective ice distribution in the sampling cross section [8].

Additional measurements of IWC and LWC were also performed with the C-IKP installed at the centerline position during the previous HAIC studies. Correlating C-IKP and particle collecting tube measurements allowed for roughly deducing the IWC distribution inside the test section.

FIGURE 1 An example of ice capture cylinder used to assess the uniformity of the cloud distribution in the test section.
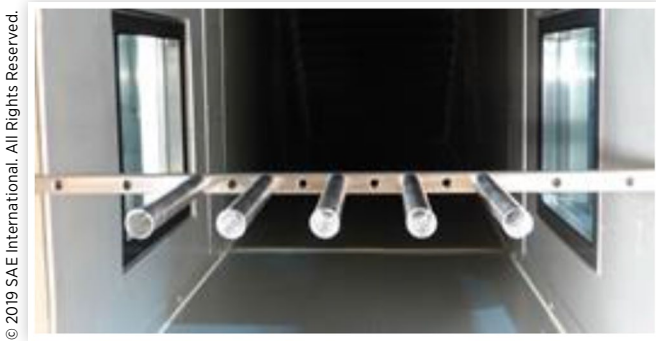
High Speed Imaging (HSI) and 2D-S (Stereo) Probes

An advanced version of standard 2D OAP, the SPEC 2D-S (Stereo) probe, with sealed optics, improved time response, and with newly developed anti-shattering arms tips, was selected as representative of spectrometers used during the HAIC in-flight measurements to identify potential discrepancies with the techniques used for the calibration of icing wind tunnels for liquid, and glaciated, conditions (HSI and PDI techniques). As imaging systems, with respect to the standard OAPs spectrometers, both HSI and 2D-S were expected to have improved sensitivity and accuracy for ice particle measurements below 100 μm and could possibly provide a better size overlap with the scattering probe for ice particle size measurements in the sub-100 μm size range.

One of the key elements for new particle image spectrometers is the quality of the images and hence, the quality and accuracy of the sizing data that have a significant dependence on the depth of field effect. Possible sources of error caused by the depth of field effect are the ambiguity of defining the particle boundaries, particles that are out of focus, and the dependency of the depth of field on particle size. Size ambiguity increases as the droplets and particles are located farther from the focal plane. It is known that the depth of field for acceptable focus decreases significantly with particle size. Small particles will appear to be out of focus at smaller distances from the focal plane than larger particles. For the 2D-S the depth of field of 100 μm diameter particles already exceeds the distance between the two probe arms, meaning that out of focus corrections will mainly impact particle sizes up to / around 100 μm, with rapidly decreasing out of focus effect beyond. For the 2D-S, out of focus particle sizes are corrected according to the method described in reference [13].

The 2D-S was designed to limit the DoF by using orthogonal views of the same particles [14]. However, this approach is reducing drastically sampling statistics and so far not been exploited routinely in the scientific community. The depth of field (DoF) in conventional OAP instruments continuously increases with increasing particle size. For larger particles the distance between the probe arms mechanically delimits theoretical DoF. Reference [3] presents the depth of field versus droplet size for different levels of intensity threshold. It is seen that for the 50% intensity threshold, the depth of field is constant for droplets larger than 100 μm. For different intensity thresholds (e.g. in OAP-2D gray probe) the depth of field differs according to the intensity thresholds. A constant depth of field is a key attribute for more accurate OAP measurements [6]. The 2D-S overlap region of the two lasers was designed to provide a small sample volume centered between the two arms of the probe. However, this approach was not used in these studies and has generally not been used, to our knowledge. The data for each channel (Horizontal and Vertical) of the 2D-S is typically used independently. In addition, small particles observed by the 2D-S have a limited DoF and are therefore only observed near the middle of the sample volume away from the probe tips. Therefore, small particles are less prone to measurement of artefacts from particle breakups on the probe tips even if designed for anti-shattering geometry. The 2D-S has 10 μm of resolution and its measurable size range is 10 μm – 1280 μm. More details in this technique can be found in reference [14].

The HSI illumination approach uses converging laser beams to mitigate effects of out-of-focus particle shadows and in the advanced image processing used to control depth of field errors which happen to be absent in the application of the 2D-S. The following section will provide the technical description of HSI technique.

HSI Probe Measurement Principle The multi-beam High-Speed Imaging (HSI) technique [15] was developed in response to the need to characterize particle fields in a wide range of liquid and icing cloud conditions. Objectives included making more reliable and accurate hydrometeor size distributions and liquid or ice water content (IWT or LWC) measurements also under mixed phase conditions or when the particles could be non spherical with a range of different shapes. One of the most critical aspects expected from this new technique was for better control for sizing and concentration measurement uncertainty due to dependence of the depth of field (DoF) on the particle size. The drawbacks linked to this dependence are the out-of-focus particles that, if not corrected with validation methods [13] or rejected, tend to be counted and measured thereby introducing errors in the measurements.

Illumination Approach and Depth of Field. The HSI instrument records high resolution (to 6 μm) digital images. It consists of an optical package with an illumination system that controls the depth of field and minimizes interference by other droplets in the optical path. To accomplish this, six compact diode lasers at 50 mW and 660 nm wavelength each with a beam expander and collimator are directed to converge toward a common beam intersection point, figure 2. The lasers

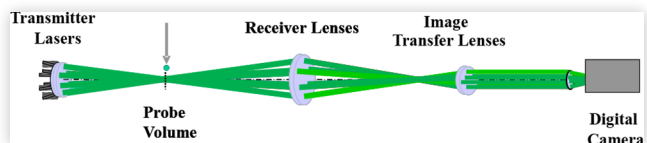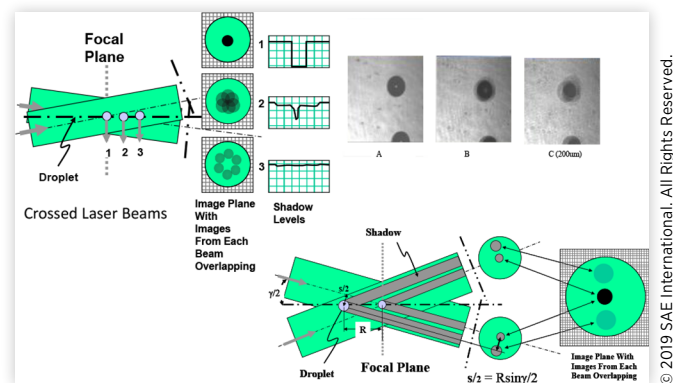**FIGURE 2** Optical layout of the multi-beam imaging approach

FIGURE 3 Schematic showing the multi-laser beam illumination.

FIGURE 4 Schematic of single beam and multi-beam illumination showing the effect of depth of field and the beam intersection angle [15].

are pulsed synchronously with the digital CMOS camera which has 480 by 640 pixels (Dalsa Genie) to capture the particle images at 300 Hz frame rate. The laser pulse durations may be selected from 12 ns to 20 µs and each laser pulse fires simultaneously and synchronously with the camera shutter opening. This approach essentially freezes the drop images and removes any sensitivity to droplet speed and angle of trajectory through the sample volume.

Figure 3 shows the basic schematic of the multi-beam illumination approach. For simplicity in the sketch are just shown two intersecting laser beams whereas the instrument has 6 converging beams. When converging beams are used, the shadows will propagate along the beam into the imaging lens. The shadows produced by each beam will only overlap when the particles are at the beam intersection and the focal plane of the receiving lens. At the beam intersection point (plane 1), the shadows from each beam will be superimposed to form a very deep shadow image of the particle. Particles at locations away from the beam intersection as shown as planes 2 and 3 will not produce sharp shadows since the shadows from each of the beams do not overlap and are illuminated by the other 5 beams. Particles that pass the beams outside of the intersection will produce out of focus shadows on one or two of the beams but the shadows will be obliterated by the other beams, figure 4. Thus, obscuration by large particles outside of the focal plane is mitigated. For a single collimated laser beam (e.g. 2D-S), if there is a large particle in the beam path but that is outside of the focal plane, the large particle may obscure the shadows of particles residing in the focal plane causing a measurement bias.

Drops detected outside of the depth of field of the receiver optics cause a significant measurement error since the sizes of the unfocused particle images will appear to be different from the true values [2, 3]. To mitigate these measurement errors, the automated image processing systems need to determine when the images are in focus based on such criteria as depth of shadow and shadow edge gradients. Although there have been several efforts to describe the variation of the apparent image size with distance on the object plane, no known reliable theoretical descriptions have been developed as yet. This is likely due to the fact that a number of parameters can affect the apparent image size and depth of field including shadow depth setting, background illumination, background
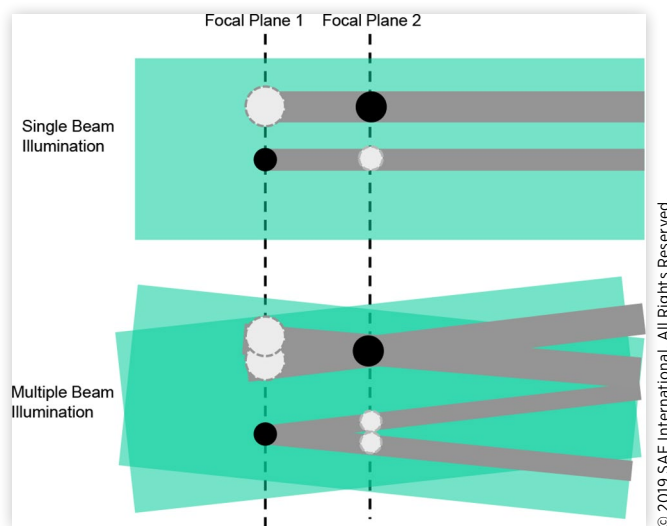
noise from out of focus images, and image processing strategies used, making the functional relationships instrument dependent.

The beam intersection angle will determine how rapidly shadow images separate for particles that are fore and aft of the focal plane of the imaging system. At the same time, the depth of field characteristics of the imaging system will determine how rapidly the shadow images move out of focus. Optimization of the multi-beam illumination approach required an analysis of the image separation rate and the imaging system depth of field (DoF). With single beam illumination, particles outside of the focal plane will begin to blur and at some point, the blur circle or Circle of Confusion (CoC) will reach an unacceptable size (Figure 3). The depth of field problem is one of the most serious sources of measurement error when using imaging systems to measure the size of small objects including ice crystal and drop size distributions.

For particle sizing, the acceptable size uncertainty usually sets the depth of field of the imaging system. Observations of larger structures such as ice particles generally will allow a larger circle of confusion and hence, a greater depth of field for the imaging system. For single beam illumination, the shadow remains as a single image, in this case a circle, but will go out of focus as indicated by blurred edges. An additional complexity occurs when observing dendritic ice crystals as the various structures are much smaller than the overall particle size and their observation will be affected by the size-dependent DoF.

With multi-beam illumination, the images will both blur and separate (Figure 4). In the design of the system, the beam intersection angle is set so that the separation of images is slower than the blur due to depth of field. In the image processing, this information is used to aid in the determination of when the images are in adequate focus or are unacceptably out of focus. Figure 5 shows an example of image frame detected by multi-beam HSI with in-focus and out-of-focus glass bead images. It is very easy for the processing

FIGURE 5 Example of shadows produced for near out-of-focus of glass beads (150 µm ± 2.6 µm) that can be easily discriminated.
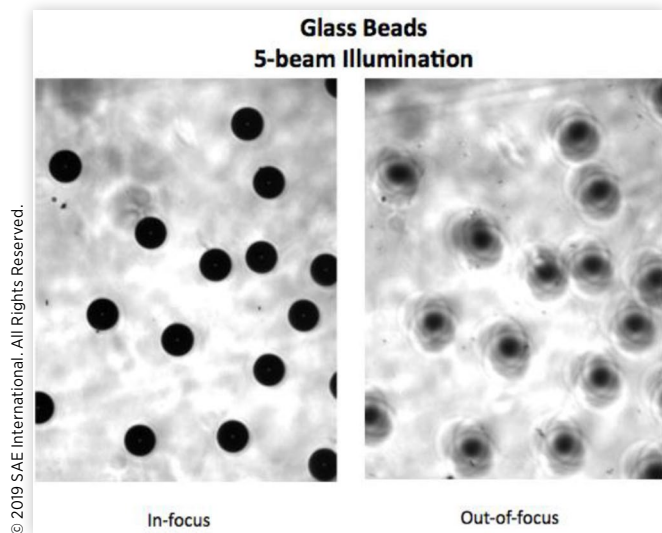
software to detect and reject the out of focus particles showing a well-defined non-overlapping shadow by measuring shadow density and edge gradients. A review of the basic analysis is reported in reference [15].

HSI Processing Software. An important parameter that must be carefully adjusted for the bright field imaging to obtain high quality imaging data and reliable depth of field size discrimination is the background illumination intensity. Figure 6 shows an in-focus image of a target using five levels of illuminations.

Even if the change in irradiance in the object plane was undetectable also from a sensible optical power meter, the effect on the image is significant. The change in the first three levels of light intensity (Figure 6a - 6c) had a positive effect on the images since the size of the circles remained constant as the background became brighter, which means there was a greater gradient between the background and the particles producing sharper edges resulting in a higher chance of measuring the correct diameters.

FIGURE 6 Five levels of illumination intensity and object detectability.
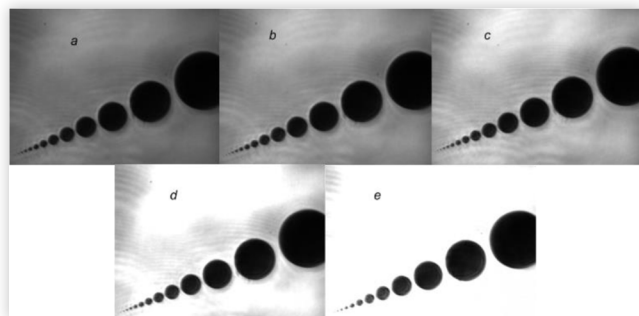
As the background light intensity is increased, there are the negative effects of the bright background. As an example, in Figure 6d, the 3.5 µm (the smallest circle to the left) dot is not visible and both 3.5 µm and 4.9 µm circles have vanished in figure 6e.

This would be acceptable if the other existing circles remained the same size because then we could use extrapolation techniques to estimate the size of smaller particles in the distribution that the imaging system cannot measure. However, by comparing the images of the circles with mean diameter of 79.2 µm ±1.7 µm from figure 6c and 6e it can be shown that the illumination in figure 6e has affected the size. In figure 7, this circle is shown in the two illumination levels and the profile of the pixel values across the diameter show that the measured size in the brighter field is smaller [15].

Optimizing of the illumination will facilitate the image processing and produce more accurate results in sizing. Given the sensitivity to the field illumination intensity, the multi-beam HSI software controls have been developed to measure local intensity over the field of view of the camera and to make adjustments to optimize the imaging system. The lasers voltage can be adjusted individually via the electronics interface and computer software to balance the intensity over the field of view. These controls set the level to what has been determined experimentally to be optimum. Since the measurement conditions can change with possible window contamination and fogging, light extinction due to ice crystal in the optical path and possibly changes in alignment, the hardware and software was designed to enable adjustment of illumination in essentially real time. A safe approach is to keep all of the pixels at a grey level about 150 (assuming the image is 8-bit) to ensure that none of the pixels are saturated. If there is a saturated pixel in the image there is a chance that a particle

**FIGURE 7** The image of a 79.2µm circle at two background illumination levels.
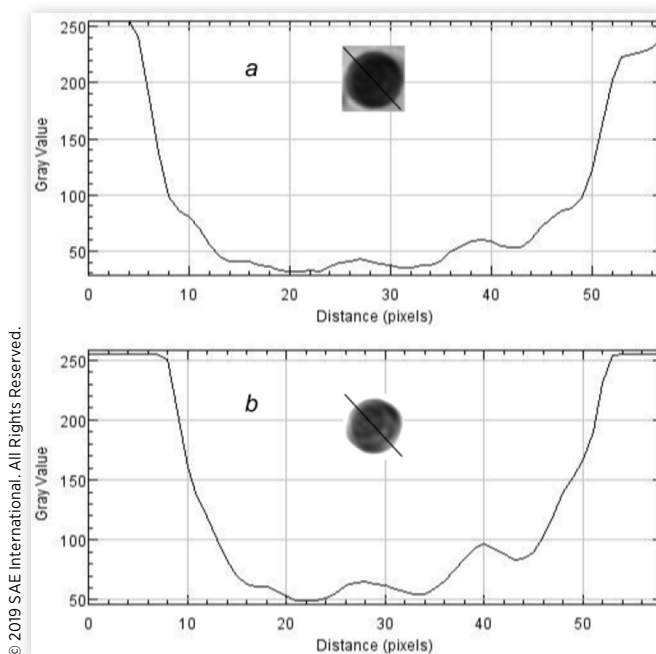
existing in that vicinity is not visible, or maybe the edge of a visible particle is washed out by the light, making it appear to be smaller.

Another important parameter of the imaging system is the volume of space that can be sampled per second. Given a similar resolution (μm/pixel) and depth of field, the sampled volume per second depends on the sensor area (number of pixels) and the frame rate (fps). For specific case of multi-beam HSI, a 480 by 640 camera at 300 fps samples approximately 92 x 106 μm² per second.

Figures 8a and 8b provides an example of measurements collected in experiments conducted to characterize the effective depth of field of multi-beam HSI imaging approach. For these experiments, glass beads of known size were placed on

FIGURE 8 Depth of field measurements used to characterize the HSI sample volume. a: Data obtained by scanning a 250 μm sphere along the imaging system optical axis. b: Measurements of the change in measured particle size with distance from the focal plane for particles in the size range of 153 μm [15].
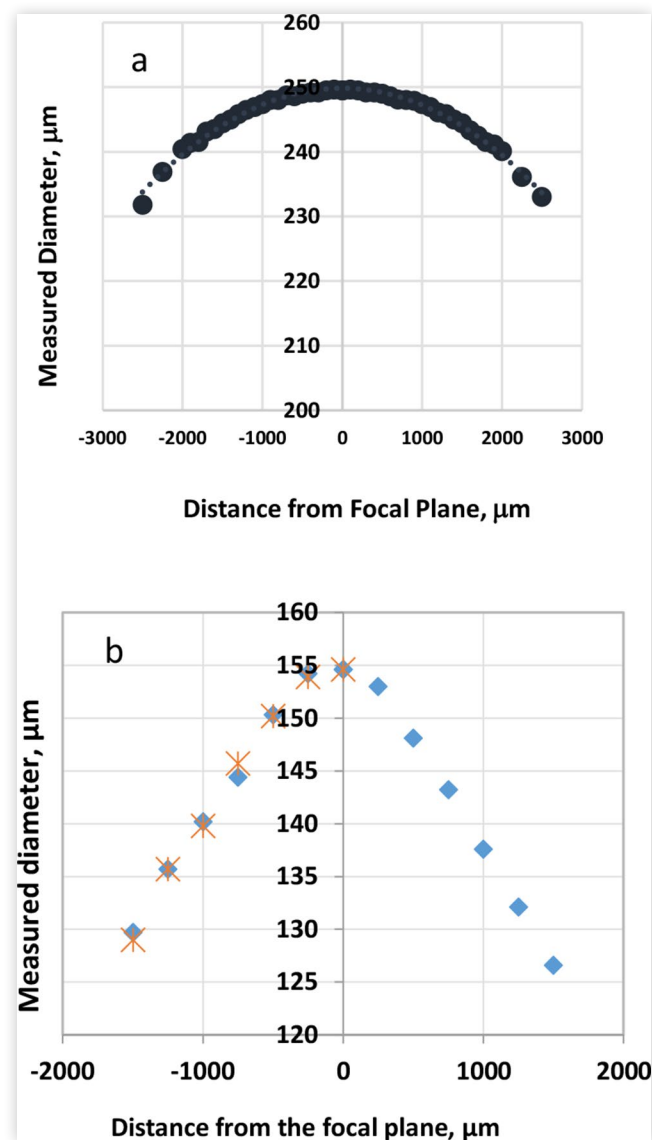

a microscope slide and traversed along the optical axis of the imaging system. Bead sizes with mean diameter of 250 μm ± 3.7 μm were used for the results in Figure 8a and 153 μm ± 2.6 μm for the results in 8b. For this last case the crosses shows the measurement repeatability. Software in-focus criteria were applied as the means for limiting the apparent depth of field. It is possible to note that the apparent image size decreases with distance from the focal plane whereas for single beam imaging, the apparent image size increases. This suggests the possibility of selecting laser beam intersection angles that minimize the change in apparent image size with distance from the focal plane.

The HSI image processing software has the ability to easily test different setup parameters (gray level, shadow gradient, etc.) and functional relationships with the depth of field as a function of the droplet diameter. These factors are included in the software image processing routines for correcting the observed object sizing. The depth of field will vary approximately linearly with particle size. In figure 9, an example of results from the experiments on depth of field as a function of object size show how the observed depth changes with increasing size. Hence, the sampling statistics are affected by this variation in the sample volume and must be corrected to obtain a reliable size distribution and mean particle size. By simply typing in new empirically derived functional forms, the results for corrected MVD and LWC are automatically updated to show whether the functional relationship was reliable or not. This has been tested by direct comparison to other sizing methods and primarily, the phase Doppler interferometer (PDI) method. After developing a suitable equation describing the depth of field effect, it has been found that the probe volume corrected (PVC) MVD values were in closer agreement to spray measurement results obtained by other means. Further refinement of the functional relationships for depth of field can be generalized over a much wider range of drop sizes.

The Adaptive Threshold method of Bradley and Roth [24] is used for wide range of conditions while providing fast processing. With this approach the inevitable variations in image intensity over the image frame are handled automatically. With the Bradley and Roth approach, the average of n×n

FIGURE 9 Experimental data acquired using multi-beam illumination showing how the apparent depth of field changes as a function of object size.
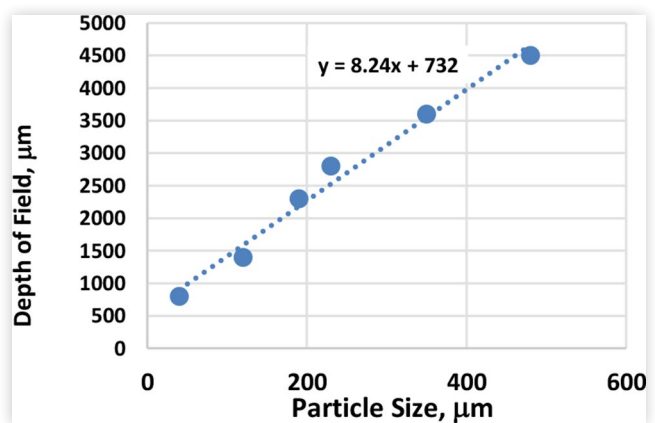
pixels using the integral image for each pixel in constant time is used to determine the local threshold for making a binary image. The improvement in the approach is that neighboring pixels on all sides are considered. When the current pixel is "*t*" percent less than this average, it is set to black. Otherwise, the pixel is set to white [25, 26].

Proprietary image processing software developed by Artium uses background noise subtraction, shadow intensity and intensity gradient to locate and characterize the particle shadow images. This software allows the evaluation of spherical and irregular shaped particles to yield various parameters describing the particle shapes obtaining useful information for characterizing ice particle habit. For each acquired image, the software first detects regions of interest (blobs), and then checks each blob against a variety of criteria. Detected shadow images produced by the particles that are within an acceptable focus allow size and shape measurements considered for statistical computations. Images are then recorded by Feret dimension, area equivalent diameter, circumference, circularity, and other parameters.

HSI method uses the concentration-based sampling where a volume of space is sampled in each shot (image area times DoF). The total number of particles measured divided by the number of images (and the sampled volume for each image, i.e. area of the sample from times the DoF) produces the concentration (number of particles divided by sum of the image volumes). Unlike probes utilizing flux-based sampling (e.g. 2D-S) the HSI probe's deadtime does not enter into calculation for the concentration.

Multi-Beam HSI Configurations Used During the HAIC Project. Differently from other imaging probes that use the CMOS camera, both HSI optical and electronic components, have been designed to fits within the standard PMS canister (figure 10). With the HSI illumination approach, it has been avoided the use of an obtrusive particle inlet system or sample tube, to minimize the effects of such an inlet, on contamination of natural hydrometeor distributions by flow effects and shattering and bouncing of artificial particles into the sample volume. The probe's arms tip shape has been designed to mitigate the particle shattering in the sampling volume.

Besides the in-situ version (C-HSI), a modular version (M-HSI) has been also arranged with transmitter (laser diodes and controller) and receiver (CMOS camera with microscope objective) have been separately assembled in different unit to permit non-intrusive measurements in small icing wind tunnel. Either C-HSI and M-HSI have the same components with the exception for M-HSI which has a high resolution, long range microscope objective (Questar QM-100) installed on the CMOS camera Questar's long range microscope optics provides high magnification and resolution at a working distance larger than the case of C-HSI. The M-HSI receiver has been designed to be located at 38 cm from the measurement volume in the centerline of the test section. With Questar's long-range microscope optics, laboratory experiments have shown M-HSI's resolution very close to the C-HSI one (3.8 instead of 3.7 µm/pixels). Figure A2 in appendix shows the calibration reticle used to characterize the resolutions. Considering that more than one pixel needs to be shadowed to resolve a particle image, the size resolution

FIGURE 10 Top: test section in the TU-BS wind tunnel during Aug-Sept 2016 testing, showing the M-PDI and M-HSI outside configuration. Bottom: C-HSI with probe volume position in the central uniform IWC region of the tunnel, in addition M-HSI (red beams) and M-PDI (green beams) sampling volumes derived laser beam intersections near the center of the tunnel at 25 mm upstream the C-HSI probe's volume.
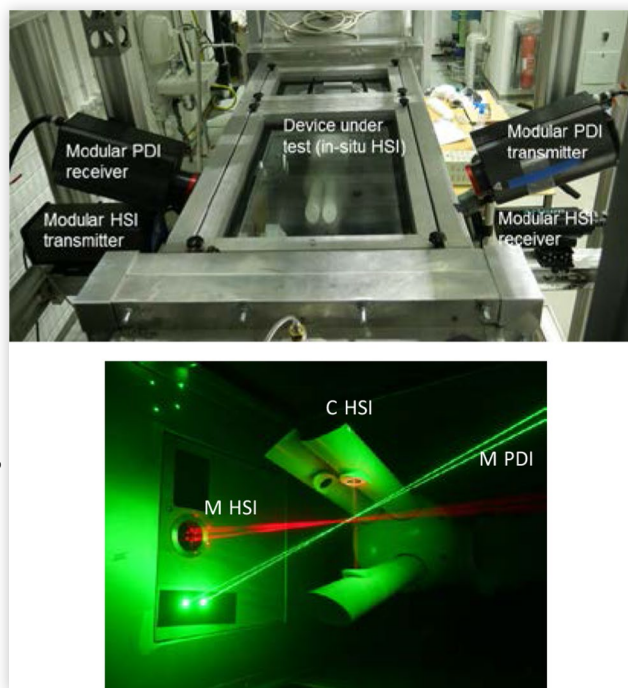
would be 8 µm for both C-HSI and M-HSI. Both instruments collect images of the particles on 640 by 480 CMOS array at 300 frames per second with sufficient resolution for obtaining the drop size and shape over the size range 8 µm - 800 µm through the magnification optimization to make full use of the CMOS array. C-HSI sample volume, as well for M-HSI, is defined by the CMOS camera pixels, image size per pixel and the DoF which is a function of particle diameter: (480 pixels x 3.7 µ/pixels) x (640 pixels x 3.7 µ/pixels) x DoF(d). Because of the large particle (droplets and crystals) size range and expected particle number density, the image processing software has been designed to detect and analyze frames with many particle images in each frame at one time. It is not uncommon to have 10 or more particles images in one frame. The transfer rates for the frames are on the order of 200 megabytes per second, which represents approximately 300 frames per second. The image processing can be in quasi-real time or be conducted off-line with the processing speed that approaches the mean data acquisition rate, which is on the order of 1000 particles/s.

Instrumentation Layout and Matrix of Conditions

In preparation of the measurement campaign an evaluation of a possible effect of the aerodynamic flow blockage due to

the installation of an individual probe canister inside the test section was concluded. A small Pitot static probe was used with and without the canister probe installed, to assess potential airflow variation in the sampling volume with respect to the case of an open test section. In addition to concentration issues related to uncertainties in the particle velocity for the 2D-S probe, it was also necessary to know if the local ice crystals' velocity was within 10% of the tunnel airspeed in order to avoid particle image distortions. The measurements with the Pitot-static probe have shown that the airspeed variability in the probe volume of each instrument was close to ±1% of the tunnel airspeed.

Due to a size and mass dependent ice crystal inertia acting on their axial velocity it was useful to know the local airspeed (or ice crystal speed). The M-PDI has been used for this scope and its measurements found a negligible effect on the axial component of the particle velocity which never decreased below 10% of the tunnel airspeed. The Phase Doppler Interferometer (PDI) can simultaneously measure droplet size and velocity for each droplet, with a size resolution to 1 µm or better. The PDI determines the particle size and speed by examining fringe patterns in the far field produced by particle light scattering [19]. Although the PDI can measure the velocity of all particles (as a laser Doppler velocimeter), it requires that the droplets are spherical or quasi-spherical to produce diameter measurements based on this assumption. Particles are rejected in the standard PDI software if their three photo-detectors signatures do not adequately match the expected signature for a sphere. In case of ice crystals with no spherical shape, the PDI cannot measure particle size since signal intensity validation becomes low and only particle's velocity can be measured. Figure 10 illustrates the instrumental configuration used in the wind tunnel for one of the experiments of this study. Due to the limited test section size, only one instrument per time has been tested for the same conditions reported in the Tabele1. The DLR-2D-S has been used to check the repeatability of the cloud conditions in terms of MMD and IWC.

After the ice crystal generation process [11], the cloud IWC is controlled by varying the frequency of a volumetric dosing machine which is linearly correlated to the ice particle mass-flow. Ice particles are supplied continuously to an oscillating sieving machine, whereby the mesh width has been selected to deliver ice crystal of a uniform well-defined upper size, rejecting bigger ice clumps. The mass flows of the sieving machine range between 4 and 46 g s^{-1}. Their ranges are independent, but for these tests, they varied between approximately 3.2 g m^{-3} and 14.2 g m^{-3} for IWC and nominally 73 - 165 µm for MMD.

The test matrix (Table 1) was designed to provide low to medium IWC to prevent potential ice crystals recirculation in the tunnel circuit at nominally constant MMDs of 73 µm - 92 µm. These prescribed MMD values were compared to the MMDs measured by the four probes during the wind tunnel tests. Airspeeds of 20 and 40 m s^{-1} representative for the available wind tunnel operating airspeeds, were chosen for testing. The most notable deficiency of the test matrix is the lack of an independent MMDs measurement to gain information on the variability. Likewise, this is true for an independent and simultaneous measurement of the IWC in order to constrain mass-size relationships for the artificial ice.

TABLE 1 Test matrix points analyzed for this experiment. TU-BS IWC calibration is derived from C-IKP measurements while the MMD is derived from HSI using the mean diameter from each blob image (description see below). The values of IWCs and MMDs are based on the average values measured by C-HSI, 2D-S, and M-HSI.

40 m s^{-1}				
Test condition no.	TU-BS IWC (g m-3)	Study IWC_ avg (g m-3)	TU-BS MMD (µm)	Study MMD_ avg (µm)
i01	3.5	2.63	111	72.33
i02	6	5.45		73.85
i03	7.61	7.6		78.65
i09	3.2	2.92		74.98
i10	7.24	9.1		71.6
		20 m s^{-1}		
I05	3.2	3.12		79.88
i06	7.12	6.73		83.45

Processing and Results

Image Processing

As with the state of the art 2D-S probe, the HSI image processing software has been developed to evaluate irregular shaped particles and to provide various parameters to describe the geometry of individual particles. Geometric information is required to characterize the ice particle habit. The software reads the average and local intensities of background of each camera frame in the area without the particles and adjust the laser intensities and/or camera gain to avoid detection of noise. With the HSI validation criteria, most of the out-of-focus images are rejected which is constrained from image shadows levels and edge gradients. Indeed, for each acquired image, the software first detects regions of interest (blobs), and then checks each blob against a variety of criteria based on the gray intensity level (0 for a black pixel and 255 for a complementary white pixel) and the shadow edge gradients, to name a few validation criteria. Real shadow images block the light, leading to decreased intensity value. For the HSI data analysis all the truncated particles are rejected and also no correction method has been applied on the particle's splashing on the probe tips due to insignificant probability to detect these particles in the small sampling volume located in the center between the probe arms with anti-shattering tip shape, as shown by frequency vs. inter-arrival plot.

The "Area (equivalent) diameter" is considered as characteristic size and the individual particle mass is calculated based on the correlation $M(Deq) = \alpha \cdot Deq\beta$, [10], assuming an ice density of 0.92 g cm^{-3}, with coefficient $\alpha=7,38 \cdot 10^{-11}$ and exponent $\beta=1,9$.

As for DLR-2D-S, only data from the horizontal arm are presented but a random testing showed good agreement between the vertical and the horizontal arm number concentrations and derived ice water content. To derive the ice number density, a combination of method M4 (for particles with d < 300 µm) and M7 (for particles with d > 300 µm) has

been used [17]. M4 uses particles with diameter L1 (= maximum pixels in TAS direction that the event lasted), "all in"-particles which undergo a spherical ring spot/out-of-focus correction [13]. M7 uses "all in" particles without Korolev correction [13] and gives the maximum dimension diameter. Typically, for the liquid number density size distributions a combination of M4 and M7 was used.

IWC was inferred using the minimum of the SPEC area-mass relationship $M = \alpha \bullet A\beta$ [17] with the coefficients α and β and an ice mass derived from a spherical particle with a constant density of ice [18]. LWC was derived assuming a spherical particle with the constant density of water. Since the phase of the particles cannot be derived from the method, the mixed phase conditions were evaluated assuming all particles are either ice or liquid, which represent a lower or upper limit of the mixed phase conditions. TWC is computed assuming all particles are liquid. Comparison between three tunnel LWCs measured by C-IKP at test section centerline and the LWC extracted from PSD measured by DLR 2D-S have been reported in figure 11 to highlight potential difference with tunnel reference values. The LWC agree within 20% at low LWC and better for higher LWC (> 1.5 g m-3).

The CNRS-LaMP 2D-S data processing has been described in detailed in Leroy et al. (2016) [9] as it has previously been used for the processing of the data sets collected during the HAIC field campaigns. The software is able to extract various size parameters form the particle images (area equivalent diameter, maximum dimension, etc.) and treats all major artefacts related to optical array probe's measurements (shattering, splashing, multiple particles in a single image, the software even recombines out-of-focus images separated by an image separator during acquisition, etc.). For truncated images, the computation of the particle's size is based on the work of Korolev and Sussman (2000) [21] and thus no criteria like "center in" or "all in" is applied: all valid images are considered for the retrieval of the particle size distribution. The size of out of focus particles is corrected
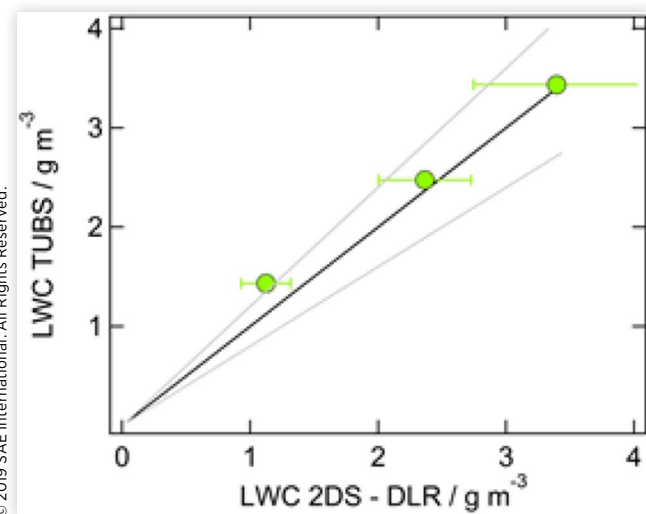
according to the work of Korolev (2007) [13]. The only difference between the analysis of the field campaign and the wind tunnel datasets lies in the shattering treatment as this artifact removal feature has been turned off for the wind tunnel measurements due to the high number of particle concentrations measured in TU-BS icing wind tunnel. For all the test conditions of this experiment, the particle inter-arrival time analyses have shown that 10% - 50% of them are in between 10^{-5} and 10^{-4} seconds. At 40 m s^{-1} of tunnel speed, this translates into interparticle distances of 0.4 mm to 4 mm, which is also the shattering domain for interparticle distances. [27]. In these conditions it is difficult to distinguish shattered from non-shattered particles. However, particle shattering may not have significantly contributed to small particle concentration due to very poor presences of large particles in the PSD.

The TU-BS Calibration

Reference values of at least IWC for each test point are available from the calibrations at the TU-BS icing wind tunnel, thereby using the C-IKP in a former study. The IWC calibrations were performed with the Cranfield University iso-kinetic probe (C-IKP) during Sept. 2015 while a first MMD characterization took place with the CIRA HSI during Dec. 2015. From these measurements, TU-BS derived the calibration curves for glaciated clouds from which tunnel IWC reference values which were selected for this study. In this section, tunnel reference values will be examined and compared to the results from other method, and attempts will be made to estimate their uncertainty.

Tunnel IWC and MMD Reference Values TU-BS derives its reference IWC from C-IKP measurements that have been developed during the HAIC project period for the calibration of icing wind tunnel for glaciated, mixed-phase and liquid spray conditions. The absolute accuracy for glaciated cloud conditions of the iso-kinetic probe has been determined in references [22, 23]. For C-IKP an evaluation of accuracy has been made using peristaltic pump to provide a reference LWC. It has been found that the C-IKP measurements are about 10 % lower than the reference value.

Figure 12 illustrates the comparison of averaged integrated IWC from 2D-S and HSI number PSD for all wind tunnel conditions and tunnel reference IWC from the C-IKP calibration work. The integrated IWC (Spectrum IWC) is an average of all IWC derived from the PSD of each instrument using the Brown and Francis, 1995 M-D relationship [10]. Due to the small MMDs range, the study of instrumentation response will be limited to the effect of variation of IWC with MMD approximately constant (Table 1).

The ratio of IWC derived from PSD to tunnel reference IWC lie between 0.75 and 1.24. 70% of the spectrum IWC are within 10% of the tunnel IWC. The reasonable agreement of the IWC derived from the microphysical probes without knowing a best mass size relationship is an encouraging result, although a larger number of lower IWC comparisons would have been desirable. Discrepancy going beyond the expected ±20% tunnel IWC uncertainty has been observed for smaller MMD test cases (conditions i01 and i10 in table 1) as shows

Comparison of LWC inferred from 2DS-DLR and the wind tunnel LWC. Grey lines represent ±20% margins, the black line is the 1:1 line

FIGURE 12 Ratio of the studied spectrum integrated and averaged IWC to the tunnel reference IWC for 20 and 40 m s-1 vs the averaged Spectrum IWC
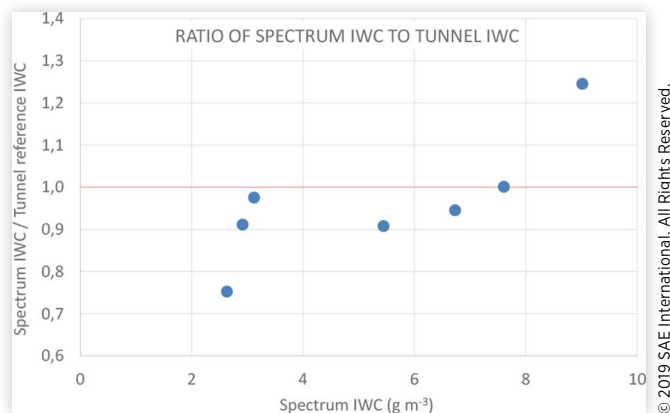
in Figure 13. The instruments agree well with the tunnel reference IWC for MMDs > 73 μm. Below this value the instruments show on average of about 25% less than the tunnel IWC (condition i01 at low reference IWC of 3.5 g cm⁻³), and on average about 24% more than the tunnel IWC (condition i10 at higher IWC (7.24 g cm⁻³)). The results allow qualifying the IWC uncertainty of about ± 25% at low MMD.

In order to evaluate the differences between different instruments Figure 14 shows a comparison of 2D-S, C-HSI, and M-HSI measurements as a function of TUBS IWC parameterization.

Most data points are situated relatively close to the one-to-one line. In general, larger differences (>20%) are observed for the higher IWC, and potentially for smaller MMDs as observed earlier (see Figure 13).

Note that the scatter in the individual IWC comparisons is within ±20% of the one-to-one line. This is a reflection of the tunnel variability, presumably resulting from turbulence generated around the ice crystal delivery pipe in the settling chamber that may cause a random migration of the tunnel IWC spatial distribution pattern over time. The actual dispersion of the tunnel could be carefully determined by calculating

FIGURE 13 Ratio of study spectrum integrated IWC to tunnel reference IWC for 20 and 40 m s-1 MMD sweep.
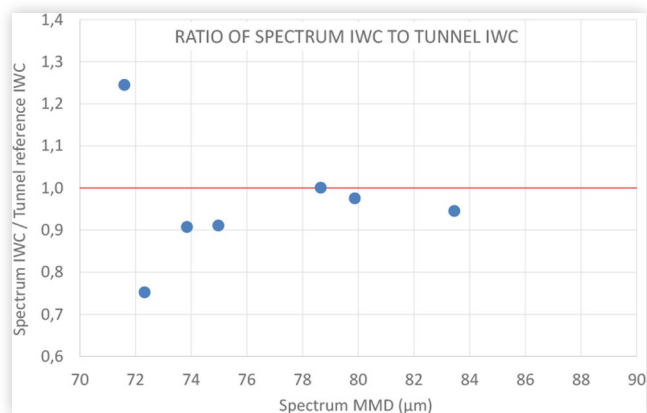
FIGURE 14 Results of HSI and 2D-S measurement methods vs tunnel reference IWC. C-IKP is used to derive tunnel reference IWCs.
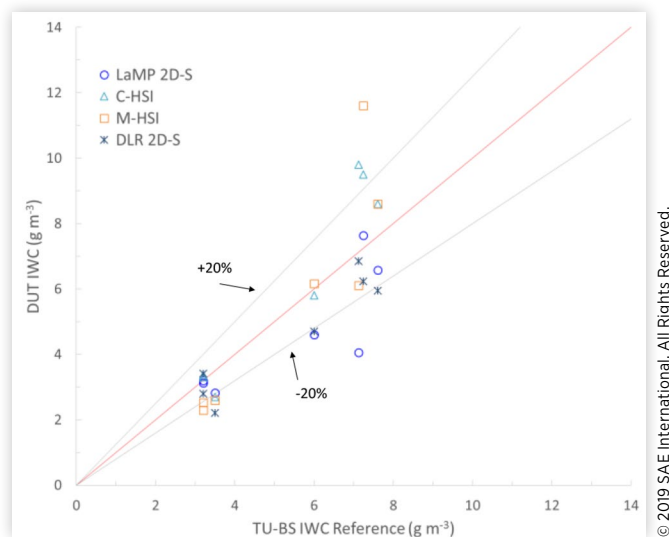
the statistics for a large number of reported conditions of the test matrix. However, due to the time available in the test campaign, only a very limited number of repetitions were conducted for the C-HSI and 2D-S measurements in this study.

The M-HSI, that has been planned to monitor the tunnel's repeatability from one evaluated probe to another, has been affected by the quality of the optical re-alignment that considerable impacts the M-HSI measurements every time when a test probe has been replaced by another probe. This has affected the detection capability of the M-HSI in the small particle size range especially for the measurements executed after the replacement of C-HSI with 2D-S probes. In that case, flawed and inconsistent data were obtained due to inadequate optics alignments.

The example result of Figure 15 compares the number density distributions between CNRS-LaMP-2D-S, C-HSI and

FIGURE 15 Particle number concentration for the test condition i03 showing the individual 2D-S, C-HSI, and M-HSI spectra. The M-HSI measurements have been simultaneously performed with the three intrusive probes sequentially installed in the wind tunnel.
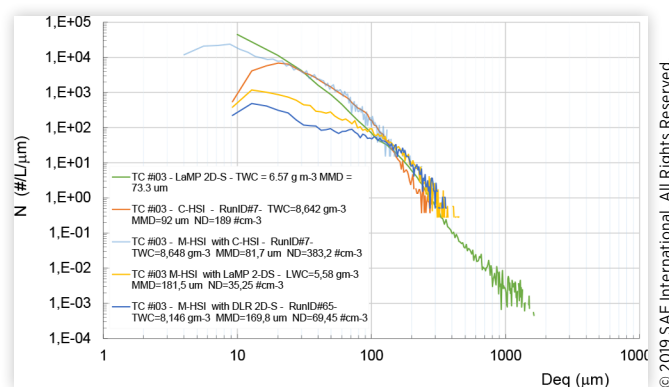
M-HSI for wind tunnel conditions i03. Three different behaviors of M-HSI curves are shown for each probe installed in the test section. There is a good overlap between C-HSI and M-HSI number density distributions in the range of 21 μm - 152 μm, but when the other probes are replaced in the test section, the agreement of M-HSI with C-HSI for the same replaced wind tunnel condition became poor and the PSD overlap is worse. This caused disagreements on MMD and IWC with the other instruments.

Since the M-HSI data have been affected by optical alignment issues, the repeatability of specific wind tunnel test conditions has been assessed comparing the response of two 2D-S probes: the CNRS-LaMP 2D-S and DLR 2D-S built with the same optics and same electronics. DLR 2D-S data have also been processed with LaMP software to avoid any bias due to the processing method and allow a direct PSD comparison. In addition, the average difference for both IWC and MMD results were compared for the two 2D-S instruments.

Figure 16 shows IWC and MMD variability over 100 seconds measurements of CNRS-LaMP and DLR 2D-S acquisitions for the same i03 condition. Average relative differences of about 9.4% and 14% have been found for IWC and MMD, respectively. Data have been sampled at 1 Hz with an average of 1 sigma standard deviation of 1.37 g m^{-3} for IWC and 3.5 μm for MMD.

Comparing the PSD for both CNRS-LaMP 2D-S and DLR 2D-S, differences are small and can be limited in the 10 μm - 30 μm and 100 μm - 300 μm size ranges as reported in the

FIGURE 16 Repeatability of tunnel condition i03 based on DLR (black plot) and LaMP (blue plot) 2D-S probes.
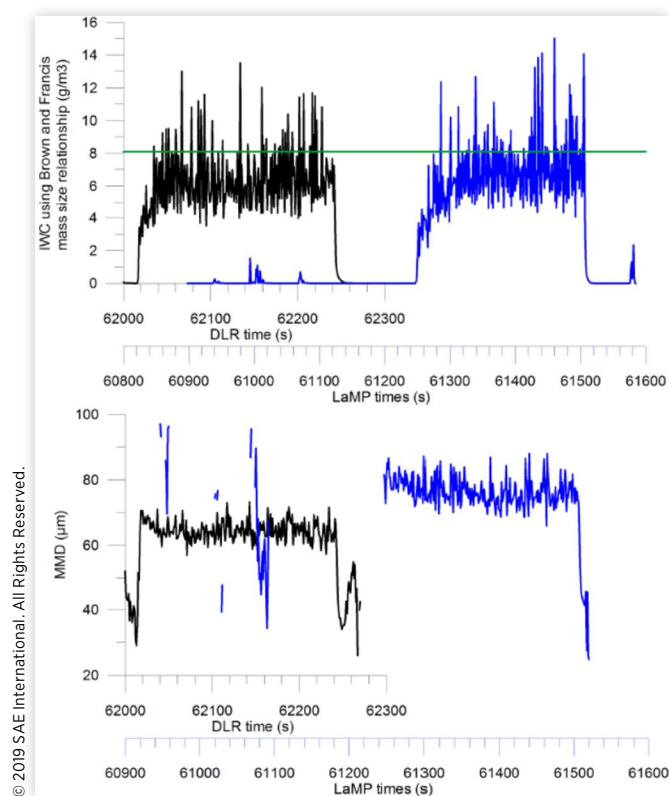
FIGURE 17 Comparison of number density distribution between LaMP and DLR 2D-S measurements (using the same LaMP method).
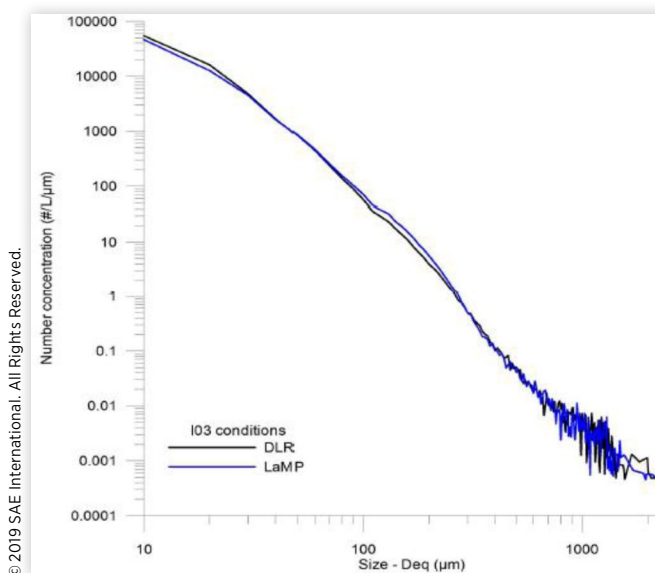
figure 17. The differences might potentially come from the limited repeatability of the wind tunnel conditions.

In the same plot of Figure 15, also the CNRS-LaMP 2D-S number density distribution has been reported (green curve) to directly compare its response with the C-HSI. A first remarkable difference is a lower concentration for diameters below 23 μm for C-HSI with respect to 2D-S. M-HSI also underestimates in the same bin size range but with concentration that is about one order of magnitude higher with respect to the C-HSI. These disagreements could be due to different aspects. Since the in-situ probes may suffer to some degree of artefact contamination due to splashing of particles off the probe tips ahead of the sampling volume, both the C-HSI and 2D-S arms are designed in different way to mitigate this effect that mainly can affect the concentration distribution for sizes below 100 μm. Furthermore, the HSI measurements are made at a small depth of filed around the center between the probe arms and will not detect particles outside of this narrow region. The sampling volume of M-HSI was located 25 mm upstream from both C-HSI and 2D-S sampling volumes (Figure 10). Both C-HSI and M-HSI have the same size resolution (3.7 and 3.8 μm) but M-HSI appears more prone to detect smaller particles with respect to the C-HSI with a 74% higher concentration in the range 4 μm - 23 μm. This increased concentration can be due to different lenses mounted on the CMOS camera for the two versions of his leading to different depths of field. The M-HSI mounts the long-distance microscope to achieve a longer working distance (560 mm instead of 156 mm as for C-HSI) with 89 mm of clear aperture (larger than 35 mm of C-HSI lens) allowing a resolution better than 3 μm with 8.7 of F/number. For the same size range, only the first two bins are available for 2D-S that collects 56% of concentration higher than M-HSI for the same size bins. It is also quite possible that the 2D-S is detecting out of focus images as small particles.

To harmonize the comparison between the probes' results, and make it independent on the data evaluation method, the same CNRS LaMP data treatments have been performed on the DLR 2D-S data. In the following section, the comparison between the probes' response will follow this criteria.

PSD Retrieval from HSI and 2D-S   Figure 18a-f

displays number density distributions for all the test conditions reporting the response of 2D-S, C-HSI and M-HSI. The test point i03 has been already shown in Figure 15. For most of the conditions there is a general overlap between the PSD of C-HSI and M-HSI from 23 μm till the maximum diameter achieved by M-HSI. Below about 23 μm, all the conditions reflect the same differences reported for the test point i03. M-HSI data highlights in general a higher variability due to lower validations with respect to the C-HSI; the C-HSI PDSs appear to be more smoothly due to a higher sampling statistics. The flat behavior of the curves below about 40 μm pointed out the low number of samples acquired for these conditions (< 5000).

Most OAPs as well as the 2D-S suffer from sizing and counting errors mainly due to out-of-focus particles that lead to over-counting and faulty sizing particularly of smaller particles [3]. Laboratory experiments, using rotating discs with spots of known diameters, showed that spectrum errors predicted for the constant depth of field part of the size spectrum are relatively small, but faulty sizing of particles smaller than about 100 μm, where the depth of field is more sensitive to size which can create large spectrum uncertainties in this size region. To limit this size error on the 2D-S, data correction has been applied by CNRS-LaMP [13, 28] to minimize this problem.

The HSI method mitigates this error by means of its illumination system that is based on multiple laser beams and the image acquisition optics. The converging laser beams from different directions highlight the in-focus particles in the sampling volume, helping to better define the system's depth of field. This analysis is limited to glaciated cloud for the sub-60 μm size range, where the uncertainty is not well known for conventional forward scattering spectrometers and optical array probes [29, 30], and where the HSI may be able to provide important insights.

An in-depth analysis of the differences observed below this size range, in particular before the C-HSI and 2D-S first crossover point (at about 30 μm for all the test point excluded the i06) is beyond the scope and practical limitations of this study due to the limitation of the tunnel to generate liquid cloud with small MVD and the availability of instruments (e.g. CDP) to use as in-flight "reference" instrument in the available time frame of the current experiment. For the larger size range (Deq>100 μm), a better agreement is found with 2D-S, especially for the test conditions i05, i09, and i10, (Figure 18c, 18e, and 18f) where the lower statistics scatters the C-HSI curve up to its maximum diameter. From this point the two PSDs show the same PSD slope even if the C-HSI rolled-off earlier than the 2D-S (at 200 μm of average Deq maximum for C-HSI and at 810 μm for 2D-S).

Typically, the valid C-HSI samples for each test point are one order of magnitude lower with respect to those

FIGURE 18 Number density distributions for all the test points (Table 1).
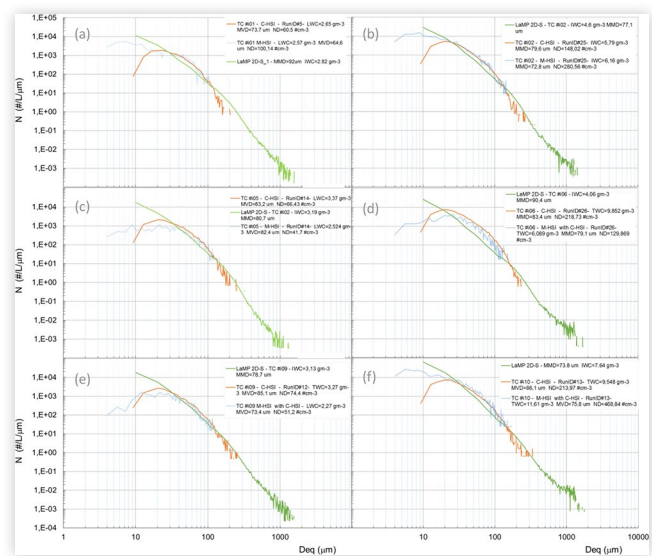
acquired by 2D-S because of a smaller sampling volume. This explains how the PSDs range of the 2D-S are always extended to larger diameters (1310 μm<Deq_max<1830 μm) if compared with those of C-HSI. Note that for all the test points reported in Figure 18, the 2D-S results drop down with respect to the C-HSI at about 30 μm and then rise at about 135 μm. The example reported in Figure 19 displayed with a dashed black curve represents a possible data combination for the size distribution in regions where the PSDs do not agree. Additional study under the liquid cloud with scattering spectrometers (e.g. CDP) would clarify if disagreement can be potentially related to the out of focus particles. Differences between the 2D-S and C-HSI raw data are showed in figure A3 and A4 of the appendix. Except for the ice crystals that passes through the focal plane of both 2D-S laser beams, many small particles are out of focus. With multi-beam HSI, most of the particles are in-focus while the out-of-focus are rejected.

FIGURE 19 Particle number concentration for test condition i09 showing the individual 2D-S and C-HSI PSD interpolated in the size range 30 μm - 135 μm.
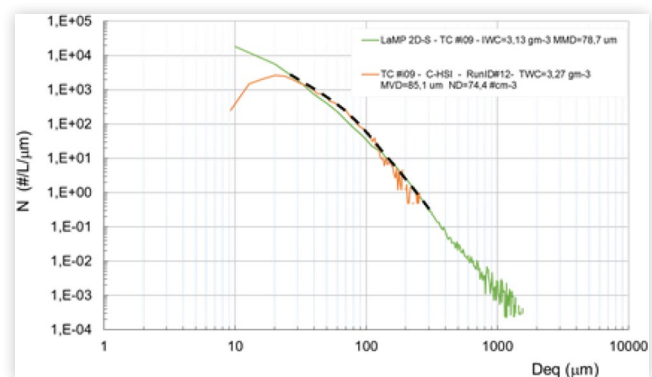
Summary of Results

For the presented experiments i01, i02, i03, i05, i06, i09 and i10 almost a complete dataset of all probes was achieved and reflects the reliability of the probes and the wind tunnel. Experiments of higher temperatures (>0 °C) could not be reproduced by the cloud probes, presumably due to melting of ice crystals in the vicinity of the sampling volume and the re-circulation effects.

Table 2 reported in the appendix, contains the full results of the study for all the instrumentation used during the experiment. For the IWC, results have been reported in terms of mean, median, standard deviation, with relative differences with respect to the tunnel's reference IWC for each test condition. For MMD results, also the mean, median, and standard deviation of the mean are displayed for each wind tunnel test point. The last two columns display the average and standard deviation of the result of all four instruments for the same test point. For most of the test points (> 70%) of all cases the integrated IWC from PSD measurements agrees with the tunnel IWC within ±20%. The MMDs range between 72 and 83 um. The largest standard deviation of the MMDs (averaged over all four probes) was found for the conditions i01 and i10.

Repeatability of each wind tunnel condition is one of the key aspects and has been considered in this study. The plot in Figure 20 provides the comparison of MMD derived from individual 2D-S (LaMP and DLR), C-HSI, and M-HSI for each test point. As reported in previous section, considering the DLR 2D-S results processed with the same CNRS-LaMP software, each test condition acquired with this probe is taken into account for the repeatability study of individual wind tunnel test conditions. It has been found that DLR 2D-S observed systematically lower MMDs than the other probes. Possible reasons may be a different operation mode of the wind tunnel during the measurements of the DLR 2D-S tunnel runs or a slightly different response of the two 2D-S probes

FIGURE 20 MMDs of seven test points from four probes are shown.
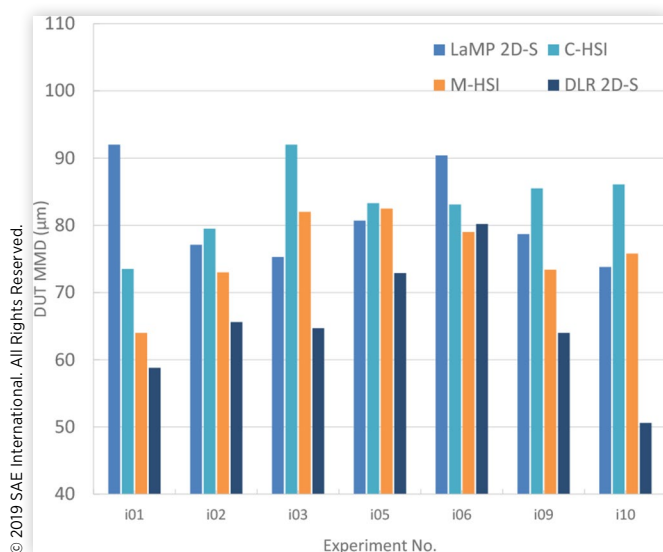
with respect to effective pixel size (identical calibration settings have been applied). The largest differences have been observed for the conditions i01 and i10 with relative difference of -23% and -35.6%, respectively. If a direct comparison between CNRS-LaMP 2D-S and DLR 2D-S is considered for the test condition i01 the relative difference would be largest (-36%). Only for the condition i05 the relative difference between CNRS LaMP 2D-S and DLR 2D-S yields the smallest value (-9.7%), which is close to the performance target and acceptance criteria defined in the tunnel calibration methodology for MMD. For all the test points the MMDs reported by C-HSI are always well below the ±10% of difference as compared to the CNRS-LaMP 2D-S except for the conditions i01 (-20%), i03 (+22%), and i10 (+16.7%). The test points i01 and i10 can be considered the least representatives in this comparative study as also highlighted in Figure 13 where larger differences with ratio of average instruments IWC to tunnel reference IWC have been found for low MMD.

Conclusions

Comparative measurements were taken at the TU-BS tunnel with the HSI and the 2D-S to provide some baseline for the performance of the new HSI based on innovative illumination approach and 2D CMOS array digital cameras designed by Artium Tech. Inc. to mitigate the particle over-sizing and related concentration artefacts due to the out-of-focus issues typically present in the 2D spectrometers images. Such baseline performance assessment was required within the HAIC research program to ensure that wind tunnel and flights with the HSI will provide reasonable data. A primary objective of such instrumentation comparisons was to characterize C-HSI response to glaciated conditions generated at different levels of IWC and respective MMD. The wind tunnel cloud parameters, formerly derived from C-IKP and C-HSI measurements, were also examined to determine the unknown MMDs' uncertainty for each glaciated condition by direct comparisons of the 2D-S and C-HSI probes' responses. The 2D-S probes used were the CNRS 2D-S and the DLR 2D-S, each one with its own data acquisition system. For both systems, the final data used for the comparison with C-HSI were processed by LaMP software developed to correct the out-of-focus images. To check the repeatability of the wind tunnel conditions, the non-intrusive HSI system was used to allow the measurements of particle images simultaneously to the probe under test.

IWC and MMDs for 7 wind tunnel test conditions of glaciated clouds at the TU-BS wind tunnel were derived from measurements of 2 optical array probes (CNRS-LaMP 2D-S and DLR 2D-S) and 2 imaging probes using CMOS cameras for imaging process (M-HSI and C-HSI). Derived IWCs from imagers were compared to recently established IWCs (from former C-IKP calibration) and the MMDs of the four imaging probes were inter-compared. For the 2D optical array probes, a single mass-size relationship (Brown and Francis, 1995) applied to the area equivalent diameter was used to calculate IWC and MMD. While MMDs ranged on average between 60 and 85 μm, IWC were probed between 3.2 and 8.3 g m⁻³.

The instruments agreed within 15% (~10 µm) for MMDs > 73 µm and 20% for IWC < 8 g m⁻³.

The average IWC values derived from the four probes were for most experiments (> 70%) in the range of ±10% of the prescribed IWC from the TU-BS wind tunnel. Up to about 14 % variability, inferred from measurements under the same nominal wind tunnel conditions, can be attributed to the wind tunnel stability/reproducibility. The instruments and the wind tunnel showed a better agreement at lower IWCs and larger MMDs (> 73 µm).

Systematic differences in the number densities of the C-HSI, the M-HSI and the two 2D-S probes were observed mainly in the size range below 30 µm and to a lesser degree at larger particle diameters (≥ 100 µm). Potential reasons for the discrepancies may be the different resolutions of the probes in the lower size range and different sampling efficiencies. The 2D-S uses a linear detector with only 128 photodiodes with approximately 10 pixel size. The C-HSI instruments with CMOS camera pixels (480 by 640 pixels) has 3.7 µm/pixel of maximum resolution resulting in more than one pixel to resolve small particle images with size below 10 µm (around 7 to 8 µm). Difference in number densities is also potentially related to different sampling method: 2D-S uses flux-based sampling, the HSI uses concentration-based sampling (figure A1). In the first sampling method, the instrument measures particles as the pass through the sampling cross-section of the instrument. With this sampling approach, deadtime is a concern as particle arrivals must be counted and the concentration then depends on the swept volume. Concentration based sampling is what happens when using pulsed lasers of imaging: a volume of space is sampled in each shot (image area times the DoF). In this case, deadtime does not enter into the concentration calculation. Results showed that IWCs and MMDs were however not affected by this discrepancy. In order to make a final assessment on the number concentrations in this size range, additional measurements with optical scattering probes, thus with a higher resolution at small particle diameters, are needed and should be included in future wind tunnel calibration tests.

The HSI is an innovative high-resolution imaging system based on illumination by multiple diode lasers and image acquisition via modern CMOS digital cameras. Currently, CMOS cameras with much larger formats and resolution (4000 x 3000 pixels) are being used in the HSI instruments. The use of high-resolution cameras requires proportionately greater storage for each image with a corresponding slowdown in the image transfer and processing activities. However, faster computers now allow close to real-time processing and storing of only the processed particle images substantially reduces storage requirements. Sampling required significant run times to accumulate numbers of particles needed to provide an adequate statistical representation of the largest particles in the distributions. An important contribution to fix this issue would be an introduction of a triggering system to increase the efficiency of data acquisition by an order of magnitude or more when sampling under dilute particle field conditions. With this upgrade, HSI has a great potential to become the standard calibration device for the wind tunnels, with the commitment to validate/quantify HSI performance when larger MMDs and/or dilute concentrations are generated in tunnels or in the atmosphere.

References

1. Joe, P. and List, R., "Testing and Performance of Two-Dimensional Optical Array Spectrometers with Greyscale," *J. Atmos. Oceanic Technol.* 4:139-150, 1987.

2. Korolev, A.V., Kuznetsov, S.V., Makarov, Y.E., and Novikov, V.S., "Evaluation of Measurements of Particle Size and Sample Area from Optical Array Probes," *J. Atmos. Oceanic Technol.* 8:514-522, 1991.

3. Korolev, A.V., Strapp, J.W., and Isaac, G.A., "Evaluation of the Accuracy of PMS Optical Array Probes," *J. Atmos. Oceanic Technol.* 15:708-720, 1998, doi:10.1175/1520-0426(1998)015.

4. Baumgardner, D. and Korolev, A., "Airspeed Corrections for Optical Array Probe Sample Volumes," *J. Atmos. Oceanic Technol.* 14:1224-1129, 1997.

5. Reuter, A. and Bakan, S., "Improvements of Cloud Particle Sizing with a 2D-Grey Probe," *J. Atmos. Oceanic Technol.* 15:1196-1203, 1998.

6. Strapp, J.W., Albers, F., Reuter, A., Korolev, A.V. et al., "Laboratory Measurements of the Response of a PMS OAP-2DC," *J. Atmos. Oceanic Technol.* 18:1150-1170, 2001.

7. Jensenl E.J., Lawson P., Baker B., Pilson B., Mo Q., Heymsfield A. J., Bansemer A., Bui T. P., McGill M., Hlavka D., Heymsfield G., Platnick S., Arnold G. T., and Tanelli S., "On the Importance of Small Ice Crystals in Tropical Anvil Cirrus," *Atmos. Chem. Phys.*, 9, 5519-5537, 2009.

8. Bansmer, S.E. et al., "Design Construction and Commissioning of the Braunschweig Icing Wind Tunnel," *Atmos. Meas. Tech.* 11:3221-3249, 2018.

9. Leroy, D., Fontaine, E., Schwarzenboeck, A., and Strapp, J.W., "Ice Crystal Sizes in High Ice Water Content Clouds. Part I: On the Computation of Median Mass Diameter from in Situ Measurements," *J. Atmos. Oceanic Technol.* 33:2461-2476, doi:10.1175/JTECH-D-15-0151.1.

10. Brown, P.R.A. and Francis, P.N., "Improved Measurements of the Ice Water Content in Cirrus Using a Total-Water Probe," *J. Atmos. Oceanic Technol.* 12:410-414, 1995, doi:10.1175/1520-0426(1995)012,0410:IMOTIW.2.0.CO;2.

11. Baumert, A., Bansmer, S., Sattler, S., Pervier, H., and Esposito, B., "Simulating Natural Ice Crystal Cloud Conditions for Icing Wind Tunnel Experiments - a Review on the Design, Commissioning and Calibration of the TU Braunschweig Ice Crystal Generation System," in *8th AIAA Atmospheric and Space Environments Conference, AIAA AVIATION Forum* (AIAA 2016-4053) doi:10.2514/6.2016-4053.

12. Leroy, D., Fontaine, E., Schwarzenboeck, A., Strapp, J.W. et al., "HAIC/HIWC Field Campaign - Specific Findings on PSD Microphysics in High IWC Regions from in Situ Measurements: Median Mass Diameters, Particle Size Distribution Characteristics and Ice Crystal Shapes," SAE Technical Paper 2015-01-2087, 2015, doi:10.4271/2015-01-2087.

13. Korolev, A.V., "Reconstruction of the Sizes of Spherical Particles from their Shadow Images. Part I: Theoretical Considerations," *J. Atmos. Oceanic Technol* 24:376-389, doi:10.1175/JTECH1980.1.

14. Lawson, R.P. et al., "The 2D-S (Stereo) Probe: Design and Preliminary Tests of a New Airborne, High-Speed, High-Resolution Particle Imaging Probe," *J. Atmos. Oceanic Technol* 23:1462-1477, doi:10.1175/JTECH1927.1.

15. Bachalo, W.D., Payne, G., Ibrahim, K., and Karami, R., "Multi-Beam Illumination for Coping with Dense Spray Using Imaging," in *ILASS-Americas 2017 Annual Conference on Liquid Atomization and Spray Systems*, Atlanta, GA, May 2017.

16. Strapp, J.W. et al., "Laboratory Measurements of the Response of a PMS OAP-2DC," *J. Atmos. Oceanic Technol.* 18:1150-1170, doi:10.1175/1520-0426(2001)018.

17. Baker, B. and Lawson, R., "Improvement in Determination of Ice Water Content from Two-Dimensional Particle Imagery. Part I: Image-to-Mass Relationships," *J. Appl. Meteor. Climatol.* 45:1282-1290, doi:10.1175/JAM2398.1. http://www.specinc.com.

18. Lawson, R. and Baker, B., "Improvement in Determination of Ice Water Content from Two-Dimensional Particle Imagery. Part II: Applications to Collected Data," *J. Appl. Meteor. Climatol.* 45:1291-1303, doi:10.1175/JAM2399.1.

19. Bachalo, W.D. and Houser, M.J., "Phase/Doppler Spray Analyzer for Simultaneous Measurements of Drop Size and Velocity Distributions", *Optical Engineering*, 23, 5, 583-590 Oct., 1984

20. Coutris, P. Leroy, D., Schwarzenboeck, A., Strapp, W. et al.; "Uncertainty of the Ice Particles Median Mass Diameters Retrieved from the HAIC-HIWC Dataset: A Study of the Influence of the Mass Retrieval Method," SAE 2019. In review.

21. Korolev A. and Sussman B., 2000: "A Technique for Habit Classification of Cloud Particles", *Journal of Atmospheric and Oceanic Technologies*, 17, n8 (august 1st, 2000).

22. Strapp, J.W., Lilie, L.E., Ratvasky, T.P., Davison, C.R., and Dumont, C., 2016. Isokinetic TWC Evaporator Probe: Development of the IKP2 and Performance Testing for the HAIC-HIWC Darwin 2014 and Cayenne Field Campaigns, in *8th AIAA Atmospheric and Space Environments Conference*, AIAA Aviation, AIAA 2016-4059. doi:10.2514/6.2016-4059.

23. Davison, C. R., Strapp, J. W., Lilie, L., Ratvasky, T. P., and Dumont, C., "Isokinetic TWC Evaporator Probe: Calculations and Systemic Error Analysis," in *2016, 8th AIAA Atmospheric and Space Environments Conference*, June 17, 2016, Washington, DC. AIAA-4060. doi:10.2514/6.2016-4060

24. Blaisot, J.B. and Yon, J., "Droplet Size and Morphology Characterization for Dense Sprays by Image Processing: Application to the Diesel Spray," *Experiments in Fluids* 39:977-994, 2005.

25. Singh, T.R., Sudipta Roy, O. Singh, I., Sinam, T., Kh. Manglem Singh, A New Local Adaptive Thresholding Technique in Binarization, *IJCSI International Journal of Computer Science Issues*, 8, Issue 6, No 2, November 2011, ISSN (Online):1694-0814 www.IJCSI.org

26. Bradley, D. and Roth, G., Adaptive Thresholding Using the Integral Image, www.derekbradley.ca/AdaptiveThresholding/index.html.

27. Korolev, A. and Field, P.R., "Assessment of the Performance of the Inter-Arrival Time Algorithm to Identify Ice Shattering Artifacts in Cloud Particle Probe Measurements," *Atmos. Meas. Tech.* 8:761-777, 2015, doi:10.5194/amt-8-761-2015.

28. Vaillant de Guélis, T., Schwarzenböck, A., Shcherbakov, V., Gourbeyre, C., Laurent, B., Dupuy, R., Coutris, P., and Duroure, C., "Study of the Diffraction Pattern of Cloud Particles and Respective Response of Optical Array Probes," *Atmos. Meas. Tech. Discuss.*, doi:10.5194/amt-2018-437, in review, 2018.

29. Brenguier J.-L., Bachalo, W.D., Chuang, P.Y., Esposito, B.M., Fugal, J., Garrett, T., Gayet, J.-F., Gerber, H., Heymsfield, A., Kokhanovsky, A., Korolev, A., Lawson, R.P., Rogers, D.R., Shaw, R.A., Strapp, W. and Wendish M., 2013: "In Situ Measurements of Cloud and Precipitation Particles. In Airborne Measurements for Environmental Research: Methods and Instruments," First edition by Wendish, M. and Brenguier, J.-L.. 2013. Wiley-VCH Verlag GmbH & Co. KGaA

30. Korolev, A., McFarquhar, G., Field, P.R., Franklin, C. et al., "Mixed-Phase Clouds: Progress and Challenges," *Meteorological Monographs* 58:5.1-5.50, 2017, doi:10.1175/AMSMONOGRAPHS-D-17-0001.1.

Contact Information

Biagio M. Esposito, Ph.D.
Work phone: +390 823 62 3945
b.esposito@cira.it

Acknowledgments

Definitions/Abbreviations

C-HSI - Canister High Speed Imaging
C-IKP - Cranfield Iso-Kinetic-Probe
CIRA - Centro Italiano Ricerche Aerospaziali
CoC - Circle of Confusion
Deq - Equivalent Diameter
DLR - German Aerospace Center
DoF - Depth of Field
IWC - Ice Water Content
LaMP - Laboratoire de Météorologie Physique
LaMP - Laboratoire de Météorologie Physique
LWC - Liquid Water Content
M - Hydrometeor Mass

M-HSI - Modular High Speed Imaging

MMD - Median Mass Diameter

OAP - Optical Array Probe.

OAP - Optical Array Probe

PDI - Phase Doppler Interferometer

PVC - Probe Volume Correction

TAS - True Airspeed

TU-BS - Technische Universität Braunschweig

Appendix

TABLE 2 Summary of the results achieved in the present experiment for IWC and MMD values for all the instrument under study.

IWC	2DS-Lamp	2DS-DLR	Modular HSI	Canister HSI	AVERAGE	STD	TUBS
i01 -mean	2,92	2,31	2,6	2,7	2,63	0,25	3,5
i01b -mean	2,83						
i01-median	2,82	2,21					
i01b-median	2,7						
i01-STD	0,58	0,54	2,1	1,19	1,10		0,53
i01b-STD	0,55						
i01-relDiff	-17%	-34%	-26%	-23%	-25%		
i01b-relDiff	-19%						
i02 -mean	4,92	4,9	6,16	5,8	5,45	0,64	6
i02-median	4,6	4,7					
i02-STD	1,1	1,3	3,1	2,12	1,91		0,90
i02-relDiff	-18%	-18%	3%	-3%	-9%		
i03 -mean	6,87	6,35	8,6	8,6	7,61	1,17	7,6
i03-median	6,57	5,95					
i03-STD	1,57	1,77	5,3	5,04	3,42		1,14
i03-relDiff	-10%	-16%	13%	13%	0%		
i05 -mean	3,12	3,47	2,524	3,37	3,12	0,42	3,2
i05-median	3,19	3,41					
i05-STD	0,48	0,61	2,45	1,34	1,22		0,48
i05-relDiff	-3%	8%	-21%	5%	-2%		
i6 -mean	4,05	6,97	6,1	9,8	6,73	2,38	7,12
i6-median	4,06	6,85					
i6-STD	0,21	1,41	2,27	2,27	1,54		1,07
i6-relDiff	-43%	-2%	-14%	38%	-5%		
i09-mean	3,3	2,76	2,3	3,3	2,92	0,48	3,2
i09-median	3,13	2,8					
i09-STD	0,81	0,81	2	1,17	1,1975		0,48
i09-relDiff	3%	-14%	-28%	3%	-9%		
i10 -mean	8,49	6,45	11,61	9,5	9,01	2,15	7,24
i10-median	7,64	6,23					
i10-STD	1,78	2,75	5,69	2,54	3,19		1,09
i10-relDiff	17%	-11%	60%	31%	24%		

MMD	2DS-Lamp	2DS-DLR	Modular HSI	Canister HSI	AVERAGE	STD
i01 -mean	92,4	58,8	64,4	73,7	72,33	15
i01-median	92	58,8	64	73,5		
i01-STD	3,35	1,77	20,4	20,5		
i02 -mean	77,5	65,5	72,8	79,6	73,85	6,3
i02-median	77,1	65,6	73	79,5		
i02-STD	2,08	3,01	19	20,4		
i03 -mean	76,1	64,8	81,7	92	78,65	11
i03-median	75,3	64,7	82	92		
i03-STD	3,96	3,06	19,9	22,7		
i05 -mean	80,8	73,1	82,4	83,2	79,88	4,6
i05-median	80,7	72,9	82,5	83,3		
i05-STD	3,1	2,6	24,8	22,6		
i06 -mean	91,1	80,2	79,1	83,4	83,45	5,4
i06-median	90,4	80,2	79	83,1		
i06-STD	3,98	5,86	22	21,9		
i09 -mean	78,9	62,5	73,4	85,1	74,98	9,6
i09-median	78,7	64	73,4	85,5		
i09-STD	2,51	6,66	21,6	21,8		
i10 -mean	73,8	50,7	75,8	86,1	71,60	15
i10-median	73,8	50,6	75,8	86,1		
i10-STD	3,36	3,27	20,2	21,9		

FIGURE A1 Sampling based on concentration-dependent and flux-dependent modes.
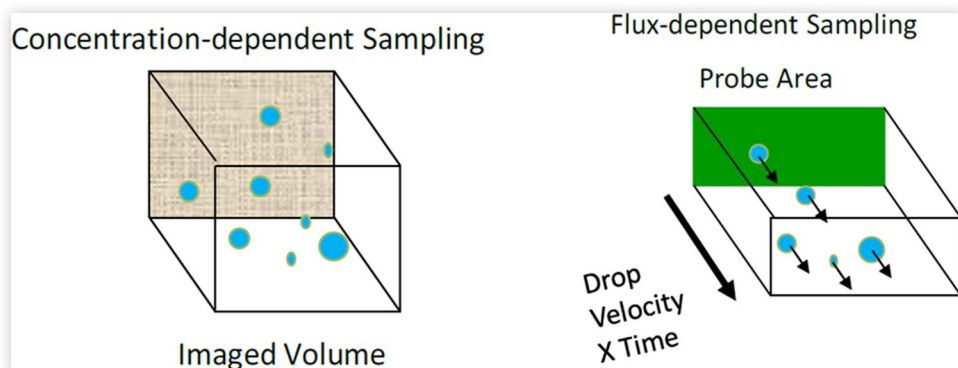
FIGURE A2 Standard calibration reticle used to characterize C-HSI and M-HSI resolutions.
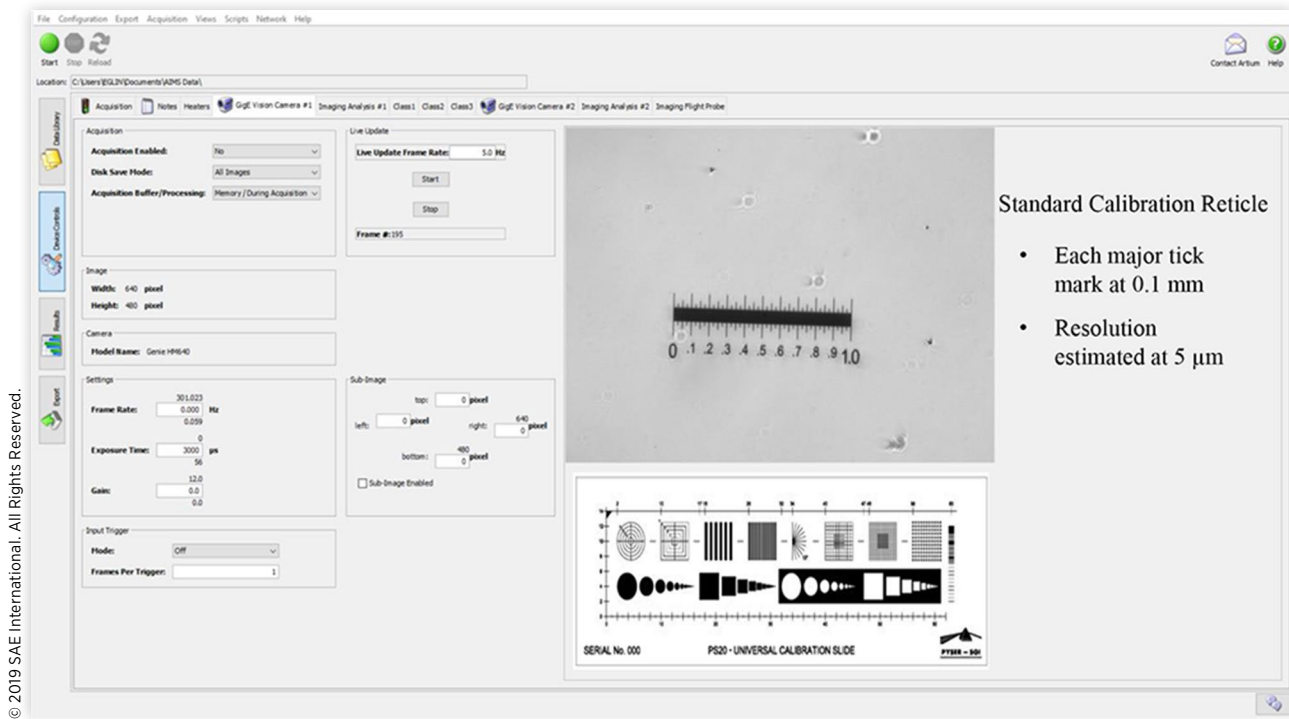
FIGURE A3 Example of 2D-S raw data showing many out-of-focus images for test conditions i08 and i02, and in focus particles from the i01 condition. In this last case, it is possible to see mainly elongated particles which are far less visible in all the out of focus images of mainly small particles (conditions i02 and i08).
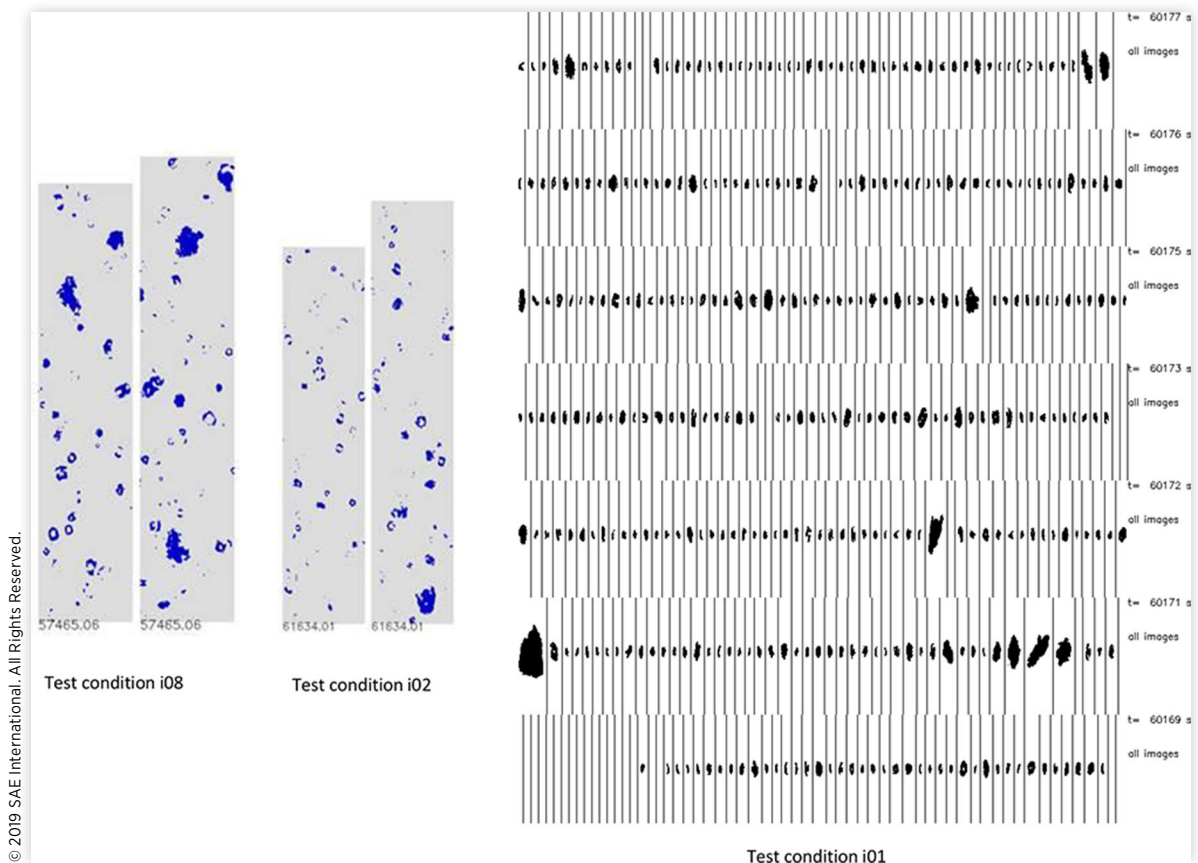
FIGURE A4   Raw data collected by C-HSI for test condition i02.
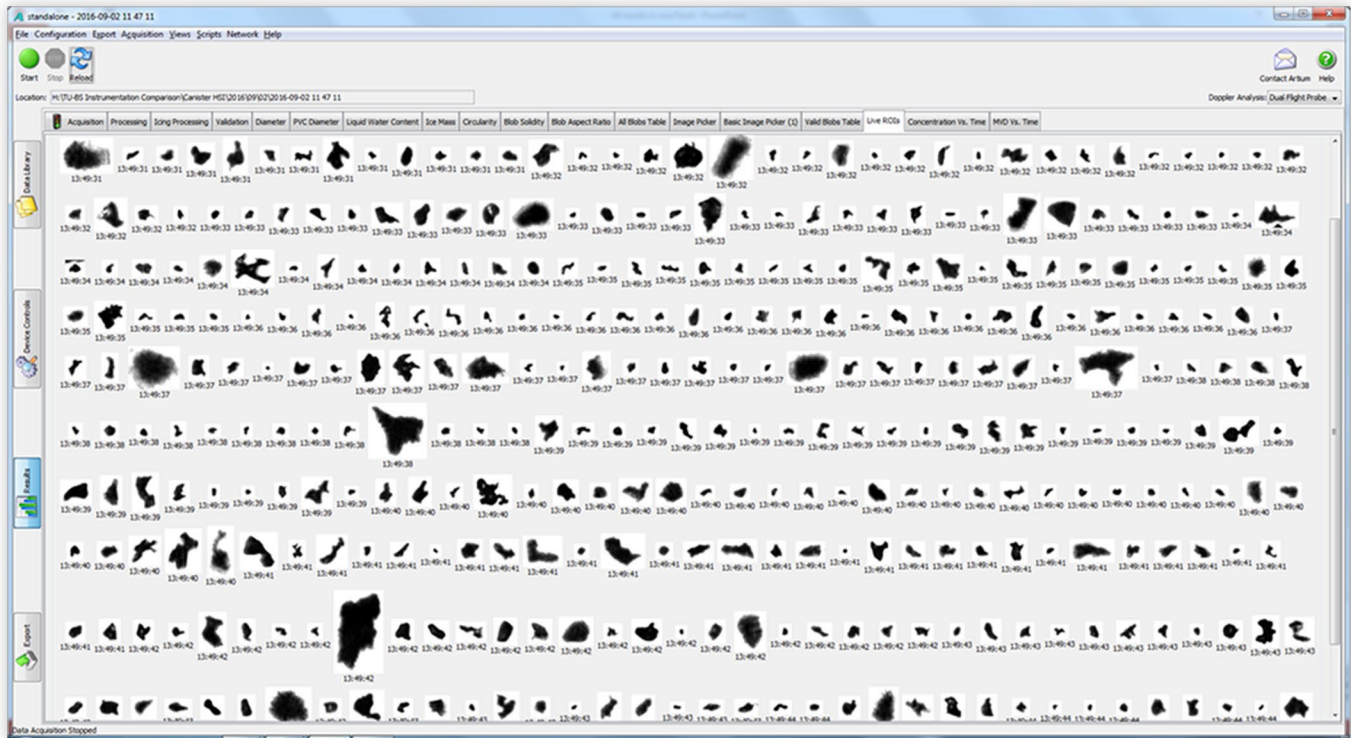
Positions and opinions advanced in this work are those of the author(s) and not necessarily those of SAE International. Responsibility for the content of the work lies solely with the author(s).